

Electroosmotic lubrication flow in constricted microchannels with a compliant wall and DLVO interactions

Subhajyoti Sahoo¹ and Ameeya Kumar Nayak^{*1}

¹Department of Mathematics, Indian Institute of Technology Roorkee, Roorkee, India

Abstract

In this paper, a novel nonlinear model for the electroosmotic transport in a constricted microchannel with a compliant lower wall is developed for applications in soft microfluidics and iontronic systems relevant to bio-inspired sensing and energy harvesting. The mathematical formulation couples the electroosmotic slip driven flow under a globally constrained electric field, pressure driven lubrication, and elastic deformation, which is modeled as a clamped KirchhoffLove thin plate. Short-range intermolecular stresses are incorporated through an extended DerjaguinLandauVerweyOverbeek (DLVO) framework that combines electrostatic double-layer repulsion and van der Waals attraction to study the nonlinear coupling between intermolecular forces, wall deformation, and electroosmotic flow in compliant microchannels. The electroosmotic flow dynamics are governed by six nondimensional parameters, i.e., wall compliance, geometric curvature, electrostatic and van der Waals strengths, the scaled Debye length, and the Dukhin number. Asymptotic analysis is performed to examine the influence of flow parameters, revealing clear physical interpretations in limiting regimes. In the stiff-wall limit, electroosmotic slip acts as a uniform offset. In the strong constriction limit, the throughput scales as $Q \sim -\sqrt{C}\mathcal{K}(Du)$ due to electric field effect, and in the narrow gap limit, wall deflection and flux suppression follows $\delta_{\max} \sim F_{\text{DLVO}}/(\mathcal{E}\mathcal{C}^2)$ and $\Delta Q \sim F_{\text{DLVO}}/(\mathcal{E}\mathcal{C}^{3/2})$, respectively. Fully coupled spectral collocation simulations confirm these predictions and capture the nonlinear feedback between pressure, deformation, and intermolecular stresses. Three distinct flow regimes emerge, i.e., a stiff-wall regime with negligible deformation, a deformation-limited regime where elastic narrowing strongly suppresses flux, and a repulsion-limited regime where DLVO forces cap wall deflection and prevent collapse. Flow rate, pressure, and wall profiles exhibit sharp nonlinear transitions with increasing compliance or curvature, marked by localization, saturation, and, in extreme cases, adverse pressure gradients and local backflow. These findings demonstrate the effect of elasticity, geometry, and molecular forces to

*Corresponding author: ameeya.nayak@ma.iitr.ac.in

jointly regulate electroosmotic lubrication and provide predictive scaling rules for the rational design of compliant electrokinetic channels operating under nanometric confinement.

Keywords: Electroosmosis, Lubrication theory, Compliant microchannels, Soft electrohydrodynamics, DLVO interactions, Intermolecular forces, Spectral collocation method

1 Introduction

Electroosmotic flow (EOF) has emerged as one of the most suitable transport mechanisms in micro and nanofluidic systems [1–4] to transport charged fluids and ions, due to the interaction of the applied potential with mobile counterions within electrical double layers (EDLs) adjacent to the solid-liquid interfaces. In the thin-EDL limit, the fluid flow in the bulk region shows a plug-like profile with interfacial slip governed by the classical Helmholtz-Smoluchowski (HS) relation. Beyond this classical regime, induced charge electroosmosis and related nonlinear electrokinetic effects have been shown to modify the near wall slip and flow structure under strong applied fields [5]. This framework underpins a wide range of applications in science and engineering, such as biosensing, chemical separations, drug delivery, and iontronic circuitry and electroosmotic diode/nanovalve devices [6–10]. Traditional microfluidic devices have primarily considered rigid channel walls with simple geometries, which enable analytical treatment of flow dynamics to optimize performance under different flow conditions. However, the shift toward soft and flexible materials in advanced microfluidics introduces new physics. Substrates such as polydimethylsiloxane (PDMS), hydrogels, and biological membranes possess elastic moduli orders of magnitude lower than those of conventional materials, allowing substantial wall deformation even under small electroosmotic stresses [11–17]. These deformations alter the local channel geometry and pressure distribution resulting in a coupled fluid structure interaction (FSI) at low Reynolds numbers, where elastic and interfacial effects dominate the inertia [18–20].

FSI in electroosmotic systems exemplifies a broader class of problems where the compliant channel wall couples strongly to confined flows. Moreover, EOF in a rigid channel wall often ignores the wall mechanics and treats it as an independent variable. However, introducing soft substrates brings wall deformation into the foreground and demands a framework to capture the bidirectional coupling. In this context, the appropriate mechanism for flow transport affected by variation in geometry and distribution of wall charge can be handled through the lubrication approximation theory [21]. Classical studies on EOF dealing with rigid surfaces primarily emphasized how the lubrication forces influence the colloidal mobility and Brownian dynamics. Recent work has analysed the stability and tunability of EOF in complex rigid wall configurations such as rotating microchannels and charge modulated periodic topographies [22, 23]. However, when elasticity is introduced into the channel walls, qualitatively new behaviors emerge [24–28]. Elastic substrates give rise to elastohydrodynamic (EHD) coupling, wherein the pressure generated by the flow deforms the walls, and this deformation, in turn, feeds back on the flow field [29–32]. Such couplings have also been observed in surface forces apparatus (SFA) and atomic force microscopy (AFM), and exploited to

extract the mechanical and rheological properties of compliant materials [33, 34]. At the level of scalar and charge transport, asymptotic analyses of dispersion in periodically modulated channels and multispecies electrolyte solutions further reveal how the microscale geometry and large scale spreading [35, 36]. These studies highlight the ubiquity of deformable interfaces in systems such as lubricated bearings, snow friction, and red blood cell motion through capillaries [19].

Deformation in compliant microchannels is studied by several authors in the context of pressure driven flows, where hydrodynamic forces within the fluid act directly on the channel walls [37–39]. In general, the pressure field associated with confined flow exerts a normal stress that deflects the channel walls, while viscous shear has less impact compared to tangential loads. The resulting deformation is resisted by the elastic restoring forces of the substrate, which are determined by the material properties such as Youngs modulus of the wall, Poisson ratio, and wall thickness. The coupling effect between the fluid stresses and solid elasticity gives rise to classical EHD interactions, in which the flow variation changes the channel geometry and alters hydraulic resistance [40, 41]. Gervais et al. [42] introduced a compliance parameter to quantify this coupling effect and demonstrated that the characteristic wall deflection can be approximated as $\delta \sim p w^4/(E h^3)$. This scaling shows that PDMS microchannels can undergo a substantial deformation even at modest pressures, leading to a nonlinear increase in hydraulic resistance. Further, Christov et al. [43] expanded this framework for flow in soft channels, which exhibit altered velocity profiles, and develop mechanical instabilities such as collapse or valve-like closure under extreme confinement. In addition to such quasi static deformations, compliant microchannels can also exhibit dynamic interfacial phenomena, for example intermittent air invasion driven by pervaporation [44]. Many recent studies have considered this theory and extended it to viscoelastic and non-Newtonian fluids, highlighting the complex rheology coupling with the compliance parameter to reshape flow resistance [45–47]. This classical understanding of EHD theory provides the foundation for the present study and is further extended to involve the effect of electrokinetic phenomena to describe soft electrohydrodynamics coupling.

Despite significant advancement in pressure driven flow in soft-lubrication micro transport mechanisms, electroosmotic counterparts remain the most sophisticated technique to transport the charged/uncharged fluids. Nevertheless, none of the classical electroosmotic theories are developed under rigid wall structures where the deformation regime hypothesis generates a considerable difference in charge transport, interfacial slip, and pressure distributions [48–52]. A few recent studies have started to explore electro or diffusioosmotic flow in compliant microchannels by demonstrating the electrokinetically augmented load bearing capacity and fluid structure instabilities in soft micro confinements [53–56]. Nevertheless, most of the studies in compliant microchannels have focused on mechanically forced or pressure driven flows [40–42], where electrokinetically induced deformation is often neglected to avoid simulation complexities. Even when compliance and electroosmosis are considered together, numerical treatments are considered for small deflections, linear elasticity, or idealized geometries, thereby missing the nonlinear feedbacks that really influence the governing phenomena associated with realistic soft microfluidic systems [43, 45, 47]. Furthermore, intermolec-

ular interactions such as van der Waals forces and electrostatic repulsion are rarely integrated with electrokinetic slip, despite their significant role under nanometric confinement and soft-interface stabilization [29, 30, 57–59]. These limitations hinder predictive modelling, obscure opportunities to deliberately harness wall compliance as a functional design parameter [15, 38, 39], and reduce the reliability of performance in iontronic, biosensing, and drug delivery devices. Related analyses have also examined for the gaseous slip flow through shallow deformable microchannels, showing that similar soft lubrication mechanisms arise in rarefied gas regimes [60]. Bridging these gaps is essential for advancing the theory of soft electroosmotic transport and can enable next-generation microfluidic systems that operate under coupled electrokinetic phenomena with the wall deformable conditions.

In this paper, a comprehensive EOF model is developed in compliant microchannels involving the electrohydrodynamic theory with wall deformation. The mathematical formulation integrates the geometry-dependent electrokinetic slip, lubrication pressure in variable gaps, elastic wall mechanics, and intermolecular interactions to capture the nonlinear feedback that arises under nanometric confinement. The nonlinear flow governing equation incorporates various critical flow governing parameters to incorporate the wall compliance factors. Asymptotic analysis with fully coupled numerical simulations is performed to analyze the coupled electrohydrodynamics and geometry to elucidate topological structural design, nonlinear theoretical modelling, and asymptotic analysis with fully coupled numerical simulations. We resolve the coupled electrohydrodynamic and structural fields to elucidate how elasticity, topological structural design, and molecular forces interact combinely to regulate the flow transport, and predict the distinct flow regimes that emerge. This framework is further extended beyond rigid wall electrokinetics and pressure driven elastohydrodynamics to predict the insight mechanism for sudden compression and reorganisation of flow structures in soft, deformable microsystems. The findings can be helpful to establish fundamental design principles reliable to micro and nanofluidic devices and can also provide the idea for the induction of wall compliance as a functional control parameter in applications ranging from biosensing and analytical separations to drug delivery and soft iontronic systems, providing a foundation for experimental validation and extension to viscoelastic or charge-regulated systems based on the requirements.

The manuscript is organized as follows. Section 2 introduces the theoretical framework for electrokinetics, hydrodynamics, elasticity, and intermolecular components of the fluid flow model, along with the nondimensional governing parameters. Section 3 presents the asymptotic analysis of the rigid-channel and small-deformation limits, providing the physical interpretation of the flow governing equations and balances. Section 4 describes the fully coupled numerical solutions and explores the nonlinear feedback between flow, geometry, and wall mechanics. Section 5 discusses the emergent transport regimes, identifies the scaling relations that collapse the dynamics, and compares them against numerical results. Finally, Section 6 summarizes the main findings, discusses their implications for soft electrokinetic systems, and highlights opportunities for future work in biosensing, drug delivery, and iontronic applications.

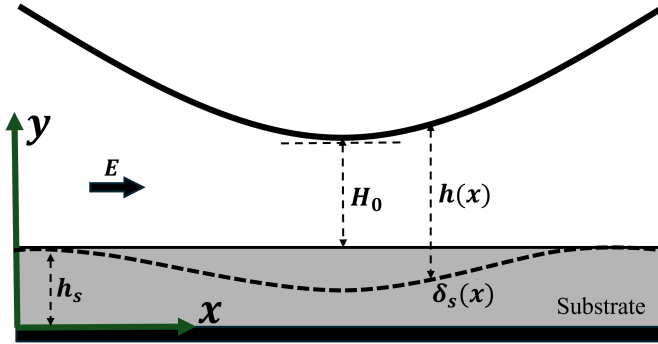


Figure 1: Schematic diagram of the electroosmotic lubrication in a constricted microchannel with a compliant lower wall. A potential drop $\Delta\phi$ drives the current through a symmetric $z:z$ electrolyte. The rigid upper wall (circular arc) creates a throat, where $E_x(x)$ focuses on enhancing Helmholtz-Smoluchowski slip. The compliant lower wall deforms under hydrodynamic pressure and DLVO disjoining stresses.

2 Theoretical Framework

In this article, a steady electroosmotic transport in a two-dimensional microchannel with a rigid, curved upper wall and a compliant lower substrate is considered. The electrolyte is a symmetric $z:z$ solution of permittivity ε and bulk conductivity σ_b , subject to a potential drop $\Delta\phi$ across a channel of length L . The undeformed gap attains its minimum value H_0 beneath the apex of the upper wall, idealized as a circular arc of radius R centered at $x = X_c$. The curvature is chosen such that the dimensionless parameter $\mathcal{C} = L^2/(2RH_0)$ is $O(1)$, representing a moderate geometric constriction. Let $\delta_s(x)$ denote the deflection of the compliant wall, so that the instantaneous gap is represented by,

$$h(x) = H_0 + \frac{(x - X_c)^2}{2R} - \delta_s(x), \quad (1)$$

with $h > 0$ by construction. The analysis assumes a slender geometry ($H_0/L \ll 1$), small slopes ($|h_x| \ll 1$), and small wall deflections ($\delta_s/H_0 \ll 1$), ensuring the validity of lubrication theory. Under these conditions, the local curvature remains weak enough that the slope condition holds across the constriction. In subsequent asymptotic reductions (Sec. 3), integrals are dominated by the throat region and are extended to infinite limits. The neglected outer contributions decay algebraically and remain asymptotically small.

2.1 Electromotive Force and its Influence on Flow Dynamics

Electroosmosis arises from the interaction of the applied electric field with the diffuse part of the electrical double layer (EDL). For $\lambda_D \ll H_0$, the EDL is thin and the slip velocity at the wall follows the Helmholtz-Smoluchowski relation

$$u_{eo}(x) = -\frac{\varepsilon\zeta}{\mu} E_x(x), \quad (2)$$

where ζ is the zeta potential and μ is the fluid viscosity. This slip condition emerges in the thin-EDL limit corresponding to $\lambda_D/H_0 \ll 1$, with nondimensionally $\kappa^* = \kappa H_0 \gg 1$. The asymptotic expansions of the Poisson-Boltzmann and Stokes equations show that the electrostatic forcing is confined to narrow $O(\lambda_D)$ layers near the charged walls, while the bulk remains electroneutral with a nearly plug-like velocity profile. For typical microfluidic conditions, $H_0 \sim 100$ nm and $c \gtrsim 10$ mM give $\lambda_D \lesssim 3$ nm and thus $\kappa^* \gtrsim 30$, justifying the thin-EDL approximation. For $\kappa^* \gtrsim 10$, the correction remains within a few percent. We adopt the convention that $E_x L / \Delta\phi > 0$ for a positive potential drop along the positive x direction. For, $\zeta < 0$ (typical for oxide or PDMS surfaces), Eq. (2) implies that electroosmotic slip is in the negative x direction, and $u_{\text{eo}}/U_\star = -E(x)$. With insulating walls, the axial current density is uniform and the total current per unit width is,

$$I = (\sigma_b h(x) + 2K_s) E_x(x), \quad (3)$$

where K_s is the surface conductance of each wall. In the thin-EDL limit with negligible surface conduction ($K_s = 0$), Eq. (3) reduces to $\sigma_b h E_x = \text{const}$, implying that $h u_{\text{eo}}$ is uniform along the channel. When K_s is finite, surface conduction slightly modifies the electroosmotic flux, characterized by the Dukhin number $Du = K_s/(\sigma_b H_0)$. The potential drop across the channel is given by,

$$\Delta\phi = \int_0^L E_x(x) dx = I \int_0^L \frac{dx}{\sigma_b h(x) + 2K_s}, \quad (4)$$

so that constricted regions contribute most to the effective electrical resistance through a harmonic-mean weighting.

2.2 Intermolecular Forces and Hydrodynamics associated with DLVO Interaction

The fluid pressure is augmented by the disjoining pressure arising from molecular interactions,

$$P(x) = p(x) + p_{\text{DLVO}}(h(x)), \quad (5)$$

where, in DLVO theory provides us,

$$p_{\text{DLVO}}(h) = 64n_0 k_B T \tanh^2 \left(\frac{ze\psi_0}{4k_B T} \right) e^{-\kappa h} - \frac{A_H}{6\pi h^3}. \quad (6)$$

Here, n_0 is the bulk ion concentration, ψ_0 is the electrostatic potential at the solid surface, κ^{-1} is the Debye length, and A_H is the Hamaker constant. The first term represents electrostatic double-layer repulsion, while the second describes van der Waals attraction. The zeta potential ζ in electroosmotic slip and the surface potential ψ_0 in DLVO interactions may differ depending on the Stern layer structure and charge distribution, but in the thin-EDL regime with fixed surface chemistry both can be treated as effective constants of comparable magnitude. Equation (6) is

appropriate for planar gaps with $h \gg \lambda_D$ and moderate potentials. It is important to mention that, the effect for the finite ion size or charge distribution are not considered here. The depth-averaged volumetric flux per unit width follows the Reynolds equation with electroosmotic slip is,

$$q(x) = -\frac{h^3(x)}{12\mu} \frac{dP}{dx} + h(x)u_{eo}(x), \quad (7)$$

which recovers the classical superposition of Poiseuille and electroosmotic contributions in the thin-EDL, neglecting the surface-conduction limit. From the application of conservation laws we can find that, $dq/dx = 0 \Rightarrow q(x) = Q$, and the pressure along the reservoirs satisfies $p(0) = p(L)$. The pressure is defined up to an additive constant, so only differences are physically relevant.

2.3 Wall Mechanics

The compliant substrate is modeled as a Kirchhoff–Love plate of thickness h_s and flexural rigidity

$$D = \frac{E_Y h_s^3}{12(1 - \nu^2)}, \quad (8)$$

where E_Y and ν are the Youngs modulus and Poissons ratio, respectively. It is assumed that $h_s/L \ll 1$ and small rotations, consistent with lubrication kinematics. Balancing fluid and elastic stresses gives

$$p(x) + p_{DLVO}(h) = D \frac{d^4 \delta_s}{dx^4}, \quad (9)$$

with clamped end conditions $\delta_s(0) = \delta_s(1) = 0$ and $\delta'_s(0) = \delta'_s(1) = 0$. This model is appropriate for thin, bonded elastomeric films, where bending dominates the torsional forces. In ultra-soft or pre-stressed membranes, an additional in-plane tension term $T\delta''_s$ can be included without altering the structure below. The wall is treated as linearly elastic, assuming small transverse deflections, negligible shear deformation, and a dominant bending response. These assumptions are consistent with the lubrication approximation and verified a posteriori in all simulations presented in Sec. 5, where $\delta_{\max} \lesssim 0.04H_0$.

The compliant wall is rigidly bonded to a stiff substrate at both ends, consistent with the clamped boundary conditions. This anchoring reflects typical microfluidic devices where soft layers (e.g., PDMS) are sealed against rigid supports (e.g., glass or silicon). Consequently, tangential wall displacement is zero at the endpoints, and displacement and stress continuity are naturally satisfied. In the lubrication limit ($H_0/L \ll 1$), tangential viscous stresses are negligible compared to normal pressure loads. Hence, the interaction between the fluid and wall occurs entirely through normal tractions.

2.4 Dimensional Analysis

Mathematical foundation is established by scaling the physical quantities used for the flow simulation to facilitate the comparison between different systems. Velocities are scaled with $U_\star = \varepsilon\zeta\Delta\phi/(\mu L)$, flux with $q_\star = U_\star H_0$, and pressure with $p_\star = \mu U_\star L/H_0^2 = \varepsilon\zeta\Delta\phi/H_0^2$. Introduce

$$x = L\tilde{x}, \quad h = H_0\tilde{h}, \quad \delta_s = H_0\tilde{\delta}_s, \quad q = q_\star\tilde{q}, \quad p = p_\star\tilde{p},$$

and drop tildes hereafter, with $x \in [0, 1]$. The geometry is given by,

$$h(x) = 1 + \mathcal{C}(x - x_c)^2 - \delta_s(x), \quad \mathcal{C} = \frac{L^2}{2RH_0}, \quad x_c = \frac{X_c}{L}. \quad (10)$$

Key dimensionless entities are

$$\kappa^* = \kappa H_0, \quad Du = \frac{K_s}{\sigma_b H_0}, \quad \mathcal{R}_e = \frac{64n_0 k_B T \tanh^2(ze\psi_0/4k_B T)}{p_\star}, \quad \mathcal{R}_v = \frac{A_H/(6\pi H_0^3)}{p_\star}, \quad \mathcal{E} = \frac{DH_0^3}{\mu U_\star L^5}.$$

Here \mathcal{E} represents the dimensionless elastic compliance, while \mathcal{R}_e and \mathcal{R}_v quantifies the electrostatic and van der Waals stresses, respectively. The dimensionless axial field follows

$$E(x) = \frac{E_x L}{\Delta\phi} = \frac{\alpha}{h(x) + 2Du}, \quad \alpha = \left(\int_0^1 \frac{dx}{h(x) + 2Du} \right)^{-1}, \quad (11)$$

which encodes the global voltage constraint and shows explicitly that the constricted region governs the electrical resistance through a harmonic-mean weighting. Using $u_{eo}/U_\star = -E(x)$, the nondimensional flux law becomes

$$Q = -\frac{h^3}{12} \frac{d}{dx} \left(p + \mathcal{R}_e e^{-\kappa^* h} - \frac{\mathcal{R}_v}{h^3} \right) - \frac{\alpha h}{h + 2Du}, \quad (12)$$

The deformable wall equation is given by,

$$p + \mathcal{R}_e e^{-\kappa^* h} - \frac{\mathcal{R}_v}{h^3} = \mathcal{E} \frac{d^4 \delta_s}{dx^4}. \quad (13)$$

Integration of Eq. (12) subject to $p(0) = p(1)$ furnishes the exact constant-flux identity:

$$Q = \frac{-\alpha \int_0^1 \frac{dx}{h^2(h+2Du)} - \frac{1}{12} \left[\mathcal{R}_e \left(e^{-\kappa^* h(1)} - e^{-\kappa^* h(0)} \right) - \mathcal{R}_v \left(\frac{1}{h^3(1)} - \frac{1}{h^3(0)} \right) \right]}{\int_0^1 h^{-3}(x) dx}. \quad (14)$$

For equal end gaps, the boundary term vanishes. In the thin-EDL Ohmic limit ($Du \rightarrow 0$), the numerator reduces to $-\alpha \int_0^1 h^{-3} dx$, giving $Q = -\alpha$, i.e., a uniform electroosmotic offset to the pressure driven flow. Physically, α acts as an electrical conductance factor set by the harmonic mean of the gap, while the denominator reflects the hydrodynamic resistance. Their competition, together with the elastic compliance \mathcal{E} and molecular forces $(\mathcal{R}_e, \mathcal{R}_v, \kappa^*)$, controls the localization of

pressure, the magnitude of wall deflection, and the throughput of the constricted microchannel. The model assumes a thin, non-overlapping EDL with fixed interfacial properties which is an extension to charge-regulated or sterically modified interfaces and can be represented by the generalized functions $\zeta(h)$, $\psi_0(h)$, or $K_s(h)$.

3 Asymptotic Analysis

Based on the theoretical framework of Sec. 2, we analyze the pressure and volumetric flux in limiting flow regimes where simplified balances expose the dominant physics. These asymptotic reductions provide transparent scaling laws and physical benchmarks that complement the full nonlinear model.

3.1 Weak-Compliance Limit (Stiff Wall)

We consider $\mathcal{E} \gg 1$, corresponding to a stiff wall with small deflections. Introduce the small parameter $\epsilon = 1/\mathcal{E} \ll 1$ and expand the pressure as,

$$p = p_0 + \epsilon p_1 + \dots, \quad \delta_s = \epsilon \delta_1 + \dots, \quad h = h_0 - \epsilon \delta_1 + \dots, \quad Q = Q_0 + \epsilon Q_1 + \dots,$$

with undeformed geometry $h_0(x) = 1 + \mathcal{C}(x - x_c)^2$ where $x_c = X_c/L$. The wall balance

$$p + \mathcal{R}_e e^{-\kappa^* h} - \frac{\mathcal{R}_v}{h^3} = \mathcal{E} \delta_s^{(4)} \quad (15)$$

yields an $\mathcal{O}(1)$ elastic response for δ_1 . At $\mathcal{O}(1)$ the bending equation is

$$\delta_1^{(4)}(x) = p_0(x) + \mathcal{R}_e e^{-\kappa^* h_0(x)} - \frac{\mathcal{R}_v}{h_0(x)^3}. \quad (16)$$

The leading-order augmented pressure is

$$P_0(x) = p_0(x) + \mathcal{R}_e e^{-\kappa^* h_0(x)} - \frac{\mathcal{R}_v}{h_0(x)^3}. \quad (17)$$

Substituting into the flux law Eq. (12) gives

$$Q_0 = -\frac{h_0^3}{12} \frac{dP_0}{dx} - \frac{\alpha_0 h_0}{h_0 + 2Du}, \quad \alpha_0 = \left(\int_0^1 \frac{dx}{h_0 + 2Du} \right)^{-1}. \quad (18)$$

Thus, in the stiff-wall limit, the electroosmotic contribution appears as a nearly uniform through-flow offset (exactly constant $-\alpha_0$ when $Du = 0$), while viscous resistance is set by the undeformed geometry h_0 . The strong viscous resistance at the throat suppresses leading-order spatial variation of the pressure under equal-reservoir conditions, making $p_0(x)$ nearly flat. Expanding the DLVO

load about h_0 ,

$$\mathcal{R}_e e^{-\kappa^* h} - \frac{\mathcal{R}_v}{h^3} = \underbrace{\mathcal{R}_e e^{-\kappa^* h_0} - \frac{\mathcal{R}_v}{h_0^3}}_{p_{\text{DLVO},0}(x)} + \epsilon \delta_1 \underbrace{\left(\kappa^* \mathcal{R}_e e^{-\kappa^* h_0} - \frac{3\mathcal{R}_v}{h_0^4} \right)}_{K_{\text{DLVO}}(x)} + \mathcal{O}(\epsilon^2). \quad (19)$$

Here $K_{\text{DLVO}}(x)$ is the incremental molecular foundation stiffness: $K_{\text{DLVO}} > 0$ corresponds to electrostatic stiffening, whereas $K_{\text{DLVO}} < 0$ indicates local softening under van der Waals attraction. The $\mathcal{O}(\epsilon)$ augmented pressure is given by,

$$P_1(x) = p_1(x) + \delta_1(x) K_{\text{DLVO}}(x). \quad (20)$$

Since the electric field is set globally by the voltage constraint, the factor α also expands as

$$\alpha = \alpha_0 + \epsilon \alpha_1 + \dots, \quad \alpha_1 = -\alpha_0^2 \int_0^1 \frac{\delta_1(x)}{(h_0(x) + 2Du)^2} dx. \quad (21)$$

The first term α_0 enforces current continuity in the undeformed geometry and the term α_1 is the global correction due to δ_1 . Expanding the flux law Eq. (12) gives,

$$q_1(x) = -\frac{h_0^3}{12} \frac{dP_1}{dx} + \frac{h_0^2 \delta_1}{4} \frac{dP_0}{dx} + \delta_1 \frac{2\alpha_0 Du}{(h_0 + 2Du)^2} - \frac{h_0}{h_0 + 2Du} \alpha_1. \quad (22)$$

The detailed explanation is provided in Appendix A.2. The second term arises from the perturbation of the hydrodynamic resistance, the third is the local EO correction (through h), and the fourth is the global EO correction (through α). In the thin-EDL Ohmic limit ($Du \rightarrow 0$), the local EO correction vanishes and only the global constant shift $-\alpha_1$ remains. The total flux is spatially uniform, $q(x) = Q = Q_0 + \epsilon Q_1$, so Q_1 follows from compatibility of Eq. (22) with boundary conditions. The deformation satisfies clamped conditions $\delta_1(0) = \delta_1(1) = \delta'_1(0) = \delta'_1(1) = 0$. In the stiff-wall regime the EO slip primarily enforces a uniform through-flow, curvature sets the geometric resistance, and DLVO forces add localized loading. The incremental stiffness K_{DLVO} acts as a stability indicator that is for the regions with $K_{\text{DLVO}} < 0$ are prone to collapse under van der Waals attraction, whereas $K_{\text{DLVO}} > 0$ implies stabilization by electrostatic repulsion. Hence, even with small deformations, the weak wall response encodes whether the constricted channel remains stable or tends to narrow, depending on the competition among the EO offset, hydrodynamic confinement, and molecular interactions.

3.2 Strong-Constriction Limit

The development of a non-planer surface morphology minimizes the strain in various levels. For the sharp constriction, when $\mathcal{C} \gg 1$, the geometry imposes a narrow throat through which current, flow, and stress are funneled. Introduce the inner coordinate $\xi = \sqrt{\mathcal{C}}(x - x_c)$, $h(\xi) = 1 + \xi^2 - \delta(\xi)$, where $\delta(\xi) \equiv \delta_s(x)$ is the dimensionless wall deflection written in the inner variable. Variations across

the throat are resolved on the $O(1)$ scale of ξ while the global channel remains slowly varying. In this reduction, integrals over the throat region are extended to $\xi \in (-\infty, \infty)$. It is important to mention that the omitted outer contribution from the geometric throat kernel is algebraically small in the inner scaling (remainder = $O(\mathcal{C}^{-5/2})$). Terms governed by the decaying wall-deflection field may be exponentially small, but the net truncation error is dominated by the algebraic tail.

3.2.1 Flux and Field Focusing

In this section, the flux focusing on the non-planer surface geometry with constriction is analyzed for hydrodynamic resistance flow. From Eq. (12) and $d/dx = \sqrt{\mathcal{C}} d/d\xi$, the inner flux law reads

$$Q = -\frac{\sqrt{\mathcal{C}}}{12} h^3(\xi) \frac{dP}{d\xi} - \frac{\alpha h(\xi)}{h(\xi) + 2Du}, \quad (23)$$

where P denotes the augmented pressure. The focusing of the electric field is encoded in the global factor α from Eq. (11). In the throat-dominated limit,

$$\alpha \sim \frac{\sqrt{\mathcal{C}}}{\pi} \sqrt{1 + 2Du}, \quad (24)$$

since $\int_{-\infty}^{\infty} d\xi [1 + \xi^2 + 2Du]^{-1} = \pi/\sqrt{1 + 2Du}$. Thus a sharper throat enhances the electroosmotic drive via electrical focusing, even as hydrodynamic resistance grows. Equation (23) shows that pressure variations in the throat depend on $Q + \alpha h/(h + 2Du)$. In the Ohmic limit ($Du \rightarrow 0$) with equal end gaps, the global closure Eq. (14) enforces $Q = -\alpha$ at leading order, so this combination vanishes and the throat pressure gradient is asymptotically small. For $Du > 0$, surface conduction weakens electroosmotic slip locally and the cancellation no longer holds, producing an $O(1)$ pressure gradient across the throat.

3.2.2 Throughput Scaling

Evaluating the throat-dominated integrals in Eq. (14) yields

$$Q \sim -\sqrt{\mathcal{C}} \mathcal{K}(Du), \quad \mathcal{K}(Du) = \frac{8}{3\pi^2} \sqrt{1 + 2Du} A(Du), \quad (25)$$

where the dimensionless throat integral is

$$A(Du) = \int_{-\infty}^{\infty} \frac{d\xi}{(1 + \xi^2)^2(1 + \xi^2 + 2Du)} = \frac{\pi}{4Du^2} \left(Du - 1 + \frac{1}{\sqrt{1 + 2Du}} \right). \quad (26)$$

Equivalently,

$$\mathcal{K}(Du) = \frac{2}{3\pi} \frac{\sqrt{1 + 2Du}(Du - 1) + 1}{Du^2}. \quad (27)$$

Consistency checks give $A(0) = 3\pi/8$ and $\mathcal{K}(0) = 1/\pi$, so that Eq. (25) reduces to $Q \sim -\sqrt{\mathcal{C}}/\pi = -\alpha$ in the thin-EDL Ohmic limit with equal end gaps. In the opposite limit $Du \gg 1$, the asymp-

totic form $\mathcal{K}(Du) \sim (2\sqrt{2}/3\pi)Du^{-1/2}$ implies a logarithmic slope of $-1/2$ for $Q/\sqrt{\mathcal{C}}$ versus Du . Here $\mathcal{K}(Du)$ encapsulates the electrokinetic efficiency of the constriction, quantifying the surface conduction (through the Dukhin number) to progressively suppresses electroosmotic throughput as interfacial charge transport short-circuits the bulk flow. The key physical insight is that the universal $\sqrt{\mathcal{C}}$ scaling of throughput reflects geometric focusing of the electric field within the constriction, which compensates with the leading order, even outweighs the increased viscous resistance in the narrowed region.

3.2.3 Wall Mechanics and DLVO Loading

The inner wall equation becomes

$$p(\xi) + \mathcal{R}_e e^{-\kappa^* h(\xi)} - \frac{\mathcal{R}_v}{h^3(\xi)} = \mathcal{E} \mathcal{C}^2 \delta^{(4)}(\xi). \quad (28)$$

The operator $\mathcal{C}^2 d^4/d\xi^4$ strongly penalizes curvature of the deflection, so that the wall response to a local load $\mathcal{L}_0(\xi)$ is sharply localized. A scaling estimate gives

$$\delta_{\max} \sim \frac{\mathcal{L}_{0,\max}}{\mathcal{E} \mathcal{C}^2}.$$

Thus, as \mathcal{C} increases, deflections become more confined but smaller in amplitude. In the Ohmic case with symmetric end gaps, the load is dominated by DLVO stresses because the throat pressure is nearly flat; for $Du > 0$, hydrodynamic pressure contributes at $O(1)$. If the end gaps are unequal, the boundary term in Eq. (14) contributes at $O(1)$ and modifies Eq. (25); for symmetric reservoirs it vanishes, leaving the universal $\sqrt{\mathcal{C}}$ scaling.

3.3 Thin-Gap Scaling Analysis

For geometrically narrow throat of the constricted channel the dominant competition is between short-range molecular forces and the elastic resistance of the compliant wall. In inner variables,

$$p(\xi) + \mathcal{R}_e e^{-\kappa^* h(\xi)} - \frac{\mathcal{R}_v}{h^3(\xi)} = \mathcal{E} \mathcal{C}^2 \delta^{(4)}(\xi), \quad h(\xi) = 1 + \xi^2 - \delta(\xi), \quad (29)$$

so a localized normal load must overcome a biharmonic operator amplified by \mathcal{C}^2 .

3.3.1 Maximum Deflection

At the throat center the load is controlled by DLVO stresses,

$$F_{\text{DLVO}} \sim \begin{cases} \mathcal{R}_e e^{-\kappa^*(1-\delta_{\max})}, & \text{electrostatic repulsion,} \\ \mathcal{R}_v, & \text{van der Waals attraction,} \end{cases}$$

leading to

$$\delta_{\max} \sim \frac{F_{\text{DLVO}}}{\mathcal{E} \mathcal{C}^2}. \quad (30)$$

The $1/\mathcal{C}^2$ dependence reflects biharmonic filtering over the inner width $\ell_c \sim \mathcal{C}^{-1/2}$; linearizing $e^{-\kappa^*(1-\delta_{\max})} \approx e^{-\kappa^*}(1 + \kappa^*\delta_{\max})$ only modifies the prefactor.

3.3.2 Throughput Reduction

With equal end gaps, the exact closure (14) gives $Q = -\alpha(I_1/I_2)$, where

$$I_1 = \int \frac{dx}{h^2(h + 2Du)}, \quad I_2 = \int \frac{dx}{h^3}.$$

A small narrowing $h = h_0 - \delta$ induces (i) a global change of α through the voltage constraint and (ii) a first-order change of the throat-dominated ratio I_1/I_2 . In the strong-constriction limit, $\alpha_0 \sim \sqrt{\mathcal{C}}$ and

$$\alpha_1 = -\alpha_0^2 \int \frac{\delta}{(h_0 + 2Du)^2} dx \sim -\sqrt{\mathcal{C}} \delta_{\max}, \quad \delta\left(\frac{I_1}{I_2}\right) \sim \delta_{\max}.$$

Therefore,

$$\Delta Q = -\alpha_1 \left(\frac{I_1}{I_2}\right)_0 - \alpha_0 \delta\left(\frac{I_1}{I_2}\right) \sim \sqrt{\mathcal{C}} \delta_{\max} \sim \frac{F_{\text{DLVO}}}{\mathcal{E} \mathcal{C}^{3/2}}. \quad (31)$$

In the Ohmic limit ($Du = 0$) the ratio $I_1/I_2 \equiv 1$ for any h , so $\delta(I_1/I_2) = 0$ exactly and $\Delta Q = -\alpha_1$. For $Du > 0$, both terms in Eq. (31) contribute at the same order. Equations Eq. (30) Eq. (31) give clear rules. Stiffening the wall ($\mathcal{E} \uparrow$) or sharpening the throat ($\mathcal{C} \uparrow$) suppresses deflection as \mathcal{C}^{-2} and mitigates flux changes as $\mathcal{C}^{-3/2}$. Stronger electrostatic or van der Waals interactions increase F_{DLVO} and hence both δ_{\max} and $|\Delta Q|$. The different powers of \mathcal{C} reflect the inner physics: deflection is set by a biharmonic response over width $O(\mathcal{C}^{-1/2})$, while throughput adjusts chiefly through the global electrical conductance encoded in α .

3.4 DLVO Limit Regimes and Force Dominance

The normal stress due to molecular interactions is modeled by,

$$p_{\text{DLVO}}(h) = \mathcal{R}_e e^{-\kappa^* h} - \frac{\mathcal{R}_v}{h^3}, \quad (32)$$

where \mathcal{R}_e quantifies double-layer repulsion, \mathcal{R}_v the Hamaker attraction, and κ^* the scaled inverse Debye length. In the present formulation p_{DLVO} loads the wall and, through the augmented pressure $P = p + p_{\text{DLVO}}$ in Eq. (12), also contributes to the axial driving.

3.4.1 Narrow-Gap Asymptotics ($h \ll 1/\kappa^*$)

Expanding the exponential term $e^{-\kappa^*h} \approx 1 - \kappa^*h + \frac{1}{2}(\kappa^*h)^2 + \dots$, we get,

$$p_{\text{DLVO}}(h) \approx \mathcal{R}_e(1 - \kappa^*h) - \frac{\mathcal{R}_v}{h^3}. \quad (33)$$

As $h \rightarrow 0$, the repulsive term tends to the constant \mathcal{R}_e , whereas the attractive term diverges algebraically like $-1/h^3$. Balancing the magnitudes of the terms gives the small-gap crossover,

$$h_c \sim \left(\frac{\mathcal{R}_v}{\mathcal{R}_e} \right)^{1/3}, \quad (\kappa^*h_c \ll 1), \quad (34)$$

below which the attractive van der Waals force dominates, leading to potential collapse or adhesion. The normal stress balance on the compliant wall can be expressed as,

$$E \delta^{(4)}(x) \approx \mathcal{R}_e - \frac{\mathcal{R}_v}{h^3}, \quad (35)$$

in the extreme narrow-gap limit. The corresponding DLVO interaction potential, defined such that $p_{\text{DLVO}} = -d\mathcal{U}_{\text{DLVO}}/dh$, is given by,

$$\mathcal{U}_{\text{DLVO}}(h) = \frac{\mathcal{R}_e}{\kappa^*} e^{-\kappa^*h} - \frac{\mathcal{R}_v}{2h^2}, \quad (36)$$

and the local stability condition $\partial^2 \mathcal{U}_{\text{DLVO}} / \partial h^2 > 0$ is equivalent to $K_{\text{DLVO}} > 0$ (defined below).

3.4.2 Wide-Gap Asymptotics ($h \gg 1/\kappa^*$)

For a large separation length, the exponential term is strongly screened and only the algebraic attraction remains

$$p_{\text{DLVO}}(h) \approx -\frac{\mathcal{R}_v}{h^3}. \quad (37)$$

At large separations the DLVO load is weak but purely attractive, so long-range softening must be offset by hydrodynamic pressure or elastic restoring stresses through

$$p(x) + p_{\text{DLVO}}(h) = \mathcal{E} \delta^{(4)}(x). \quad (38)$$

This limit is analogous to thin-film stability problems where the elastic restoring force replaces surface tension as the regularizing mechanism.

3.4.3 General Crossover and Incremental Stiffness

Away from the small-gap approximation, the crossover gap satisfies,

$$\mathcal{R}_e e^{-\kappa^*h_c} = \frac{\mathcal{R}_v}{h_c^3}, \quad (39)$$

which reduces to $h_c \sim (\mathcal{R}_v/\mathcal{R}_e)^{1/3}$ when $\kappa^* h_c \ll 1$. The local flow stability can be achieved with the incremental DLVO stiffness which is defined by,

$$K_{\text{DLVO}}(h) \equiv -\frac{d}{dh} p_{\text{DLVO}}(h) = \kappa^* \mathcal{R}_e e^{-\kappa^* h} - \frac{3\mathcal{R}_v}{h^4}. \quad (40)$$

Regions with $K_{\text{DLVO}} > 0$ are stiffened by electrostatic repulsion, whereas $K_{\text{DLVO}} < 0$ indicates van der Waalsdriven softening and potential collapse. Setting $K_{\text{DLVO}} = 0$ defines a marginal stability thickness,

$$h_s \sim \left(\frac{3\mathcal{R}_v}{\kappa^* \mathcal{R}_e} \right)^{1/4}, \quad (41)$$

valid for $\kappa^* h_s \ll 1$.

3.4.4 Force-Dominance Interpretation

The equilibrium of molecular and elastic stresses is governed by

$$E \delta^{(4)}(x) \approx \mathcal{R}_e e^{-\kappa^* h} - \frac{\mathcal{R}_v}{h^3}. \quad (42)$$

The ratio is given by,

$$\Pi(h) = \frac{\mathcal{R}_e e^{-\kappa^* h} h^3}{\mathcal{R}_v}, \quad (43)$$

characterizes the dominance of competing interactions. For $\Pi \gg 1$, double-layer repulsion dominates, For $\Pi \ll 1$, van der Waals attraction governs and $\Pi \sim 1$ marks the onset of bistability, analogous to the primary minimum in classical DLVO potential wells.

Since the p_{DLVO} terms enters both the wall equilibrium and the axial flux law through $P = p + p_{\text{DLVO}}$, the parameters \mathcal{R}_e , \mathcal{R}_v , and κ^* (representing surface charge chemistry, Hamaker attraction, and electrolyte screening) jointly determine whether a compliant microchannel stabilizes at a finite mean gap or collapses under attraction. These limiting relations provide rigorous analytical benchmarks for interpreting the fully coupled results developed in Secs. 23.

4 Numerical Methodology and Validation

The coupled flow governing equations compliant wall with electroosmotic lubrication, defined by the flux relation (Eq. (12)), the wall equilibrium condition (Eq. (13)), and the geometric constraint (Eq. (10)) constitute a stiff, nonlinear boundary value problem that integrates hydrodynamic transport, elastic deformation, and intermolecular interactions. The intrinsic stiffness of the system arises from the fourth-order nature of the wall deflection equation, the exponential dependence of the electrostatic double-layer repulsion, and the algebraic singularity associated with van der Waals attraction. Spatial discretization is performed using a Chebyshev spectral collocation scheme, and the resulting set of nonlinear equations are solved iteratively using a NewtonRaphson method to ensure rapid convergence and numerical stability.

4.1 Discretization and Residuals

The interval $x \in [0, 1]$ is mapped to $N + 1$ ChebyshevGaussLobatto nodes defined by,

$$x_j = \frac{1}{2} \left(1 - \cos(j\pi/N) \right), \quad j = 0, \dots, N,$$

which cluster near the ends and permit accurate enforcement of clamped boundary conditions. At the collocation points,

$$\delta_s(x_j) \approx \delta_j, \quad p(x_j) \approx p_j, \quad h_j = 1 + \mathcal{C}(x_j - x_c)^2 - \delta_j,$$

and obtain derivatives via Chebyshev differentiation matrices D, D^2, D^4 (constructed directly on $[0, 1]$; equivalently scaled from $[-1, 1]$). ClenshawCurtis weights w_j provide high-order quadrature. The beam balance at node j is found to be,

$$\mathcal{R}_1^{(j)} = p_j + \mathcal{R}_e e^{-\kappa^* h_j} - \frac{\mathcal{R}_v}{h_j^3} - \mathcal{E}[D^4 \boldsymbol{\delta}]_j,$$

and the flux law is enforced as,

$$\mathcal{R}_2^{(j)} = -\frac{h_j^3}{12} [D\mathbf{P}]_j - \frac{\alpha h_j}{h_j + 2Du} - Q, \quad P_j = p_j + \mathcal{R}_e e^{-\kappa^* h_j} - \frac{\mathcal{R}_v}{h_j^3}.$$

The global electroosmotic factor α is recomputed from the voltage constraint at each outer iteration as,

$$\alpha = \left(\sum_{j=0}^N \frac{w_j}{h_j + 2Du} \right)^{-1}.$$

The unknowns $(\boldsymbol{\delta}, \mathbf{p}, Q)$ are obtained by considering the clamped wall conditions $\delta(0) = \delta(1) = 0$, $\delta'(0) = \delta'(1) = 0$ by imposed in row replacement. The reservoirs are taken at the same gauge pressure (set to zero), which is enforced by $p(0) = p(1) = 0$. The clamped boundary conditions on wall deflection, $\delta_s = \delta'_s = 0$ at both ends, are enforced by row replacement in the Chebyshev matrices. Since the wall is rigidly anchored to the substrate, axial displacement vanishes at the ends. Under lubrication scaling ($H_0/L \ll 1$), tangential viscous stress is subdominant to normal pressure load; thus only normal tractions contribute appreciably to fluidstructure interaction, and no explicit tangential-stress continuity is required at the wall ends.

4.2 Nonlinear Solution algorithm

At Newton step n , the updated values of $(\Delta\boldsymbol{\delta}, \Delta\mathbf{p}, \Delta Q)$ are represented by,

$$\mathcal{J}^{(n)} \begin{bmatrix} \Delta\boldsymbol{\delta} \\ \Delta\mathbf{p} \\ \Delta Q \end{bmatrix} = -\mathcal{F}^{(n)}, \quad \begin{bmatrix} \boldsymbol{\delta} \\ \mathbf{p} \\ Q \end{bmatrix}^{(n+1)} = \begin{bmatrix} \boldsymbol{\delta} \\ \mathbf{p} \\ Q \end{bmatrix}^{(n)} + \alpha_{\text{step}} \begin{bmatrix} \Delta\boldsymbol{\delta} \\ \Delta\mathbf{p} \\ \Delta Q \end{bmatrix},$$

with $0 < \alpha_{\text{step}} \leq 1$ chosen by line search. We employ an inexact Newton scheme where, α is recomputed from the current h at each outer iteration and held fixed within the Jacobian. Including the sensitivity

$$\frac{\partial \alpha}{\partial h_j} = \alpha^2 \frac{w_j}{(h_j + 2Du)^2}$$

in the Jacobian yields indistinguishable solutions with modestly fewer iterations. A line-search safeguard $h_j > h_{\min}$ (typically $h_{\min} = 10^{-4}$) avoids transient van der Waals singularities; converged solutions remain well above this floor. Initial guesses use the stiff-wall limit ($\delta \equiv 0$, with P_0 and Q from the corresponding ODE), and strongly nonlinear cases are obtained by homotopy continuation in \mathcal{R}_v , \mathcal{R}_e , or \mathcal{E}^{-1} . Convergence condition is given by,

$$\|\mathcal{F}^{(n)}\|_{\infty} < 10^{-8}, \quad \|\Delta\boldsymbol{\delta}\|_{\infty}, \|\Delta\mathbf{p}\|_{\infty} < 10^{-8}, \quad |\Delta Q| < 10^{-10}.$$

In general, residuals decay rapidly and tolerance is typically reached within 1020 iterations and the convergence is quadratic in weakly nonlinear regimes and remains superlinear under strong DLVO forcing with under-relaxation.

4.3 Validation and Convergence

We validate our result with the analytic solution obtained through asymptotic analysis justifying the conservation of mass. In the stiff-wall limit ($\mathcal{E} \gg 1$), the discrete solution reproduces the one-dimensional ODE

$$Q = -\frac{h_0^3}{12} P'_0(x) - \frac{\alpha_0 h_0(x)}{h_0(x) + 2Du}, \quad \alpha_0 = \left(\int_0^1 \frac{dx}{h_0 + 2Du} \right)^{-1}, \quad h_0 = 1 + \mathcal{C}(x - x_c)^2,$$

with $P_0(0) = P_0(1) = 0$, to within 1% (Fig. 2a). Mass conservation is verified by computing the local flux

$$q(x) = -\frac{h^3(x)}{12} P'(x) - \frac{\alpha h(x)}{h(x) + 2Du},$$

which remains constant and lies within 10^{-6} (Fig. 2b). In the Ohmic limit $Du = 0$ with equal end gaps, the identity $Q = -\alpha$ holds exactly and is recovered numerically. Grid-refinement studies confirm spectral accuracy: beyond $N = 100$, changes in δ_{\max} , Q , and p_{\max} fall below 0.01% (Table 1); endpoint pressures satisfy $|p(0)|, |p(1)| < 10^{-8}$.

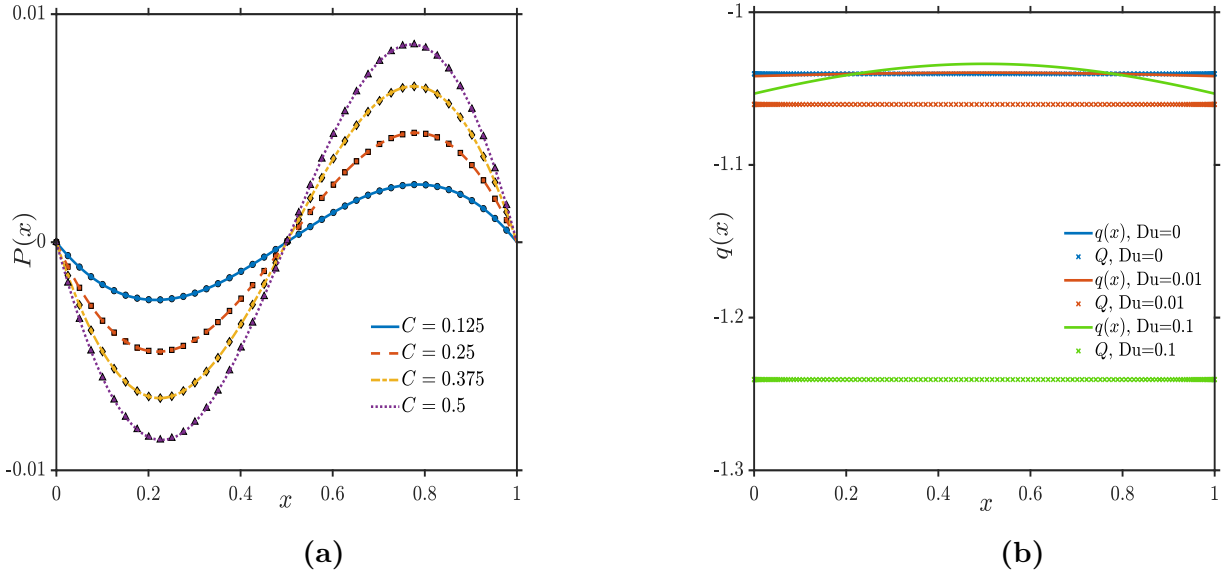


Figure 2: Validation of the numerical scheme. (a) augmented pressure $P(x)$ from the collocation solver (markers) compared with the 1D asymptotic solution for varying curvature $C \in \{0.1, 0.2, 0.3, 0.5\}$ for the case of stiff-wall limit ($\mathcal{E} \rightarrow \infty$). (b) the local flux $q(x) = -h^3 P'(x)/12 - \alpha h/(h + 2Du)$ is spatially constant and matches the domain value Q for $Du = 0, 0.01, 0.1$ (solid curves), with deviations.

Table 1: Grid-refinement study demonstrating spectral convergence. Beyond $N = 100$ collocation points, changes in δ_{\max} , Q , and p_{\max} fall below 0.01%.

Collocation points N	δ_{\max}	Q	p_{\max}
60	0.037518	1.00374	0.19834
80	0.037492	1.00351	0.19839
100	0.037489	1.00347	0.19840
120	0.037488	1.00346	0.19841

5 Results and Discussion

The numerical simulated results of the coupled electrohydrodynamic elastic system are validated with the asymptotic analyses presented in Sec. 3 and elucidate the physical mechanisms associated with the electroosmotic lubrication in constricted microchannels with compliant walls. The results demonstrated that wall elasticity, geometric focusing, and intermolecular (DLVO) forces together dictate the transport behavior through a sequence of distinct regimes: (i) a stiff-wall regime, characterized by negligible deformation and an approximately linear relation between flux and applied voltage; (ii) a deformation-limited regime, where elastic narrowing of the channel constrains flow; and (iii) a repulsion-limited regime, in which DLVO repulsion prevents collapse under strong electrostatic forcing. The transitions between these regimes arise from nonlinear coupling between electroosmotic slip, hydrodynamic pressure, and elastic deflection.

5.1 Compliance-controlled regimes

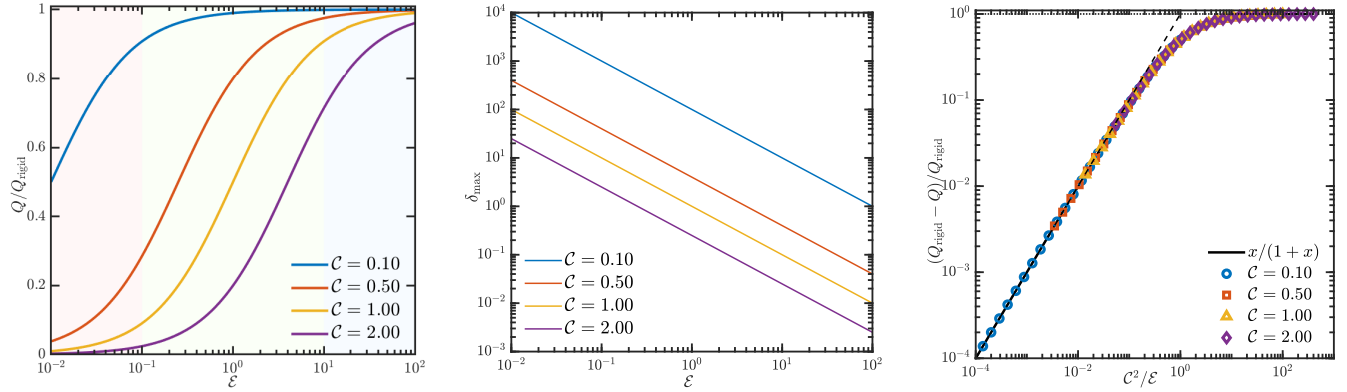


Figure 3: (a) Normalized flux Q/Q_{rigid} versus wall stiffness \mathcal{E} for different curvature values C , showing a monotonic increase toward the rigid wall limit and saturation at a repulsion-limited plateau for soft walls. (b) Rescaled maximum deformation $C^2 \delta_{\text{max}}$ versus inverse stiffness $1/\mathcal{E}$, confirming $\delta_{\text{max}} \propto (\mathcal{E}C^2)^{-1}$. (c) Normalized flux deficit $(Q_{\text{rigid}} - Q)/Q_{\text{rigid}}$ versus C^2/\mathcal{E} , demonstrating collapse across curvatures and identifying C^2/\mathcal{E} (or equivalently $(\mathcal{E}C^2)^{-1}$) as the key dimensionless control parameter.

Figure 3(a) shows the normalized volumetric flux Q/Q_{rigid} as a function of wall stiffness \mathcal{E} for various geometric curvatures C . The flux increases monotonically with \mathcal{E} , reflecting the growing influence of wall compliance on the hydrodynamic resistance as the wall becomes softer (smaller \mathcal{E}). At large \mathcal{E} , the behavior approaches the rigid wall limit, where flow is primarily electroosmotic and scales linearly with the applied potential. As \mathcal{E} decreases, deformation constricts the throat region, increasing local pressure and reducing throughput. At sufficiently low stiffness, the curve saturates to a finite plateau, marking the onset of the repulsion-limited regime where the DLVO repulsive stress balances the Maxwell and hydrodynamic pressures. The sharpening of this transition with increasing curvature highlights that geometric confinement amplifies the coupling between electrostatic and elastic effects.

Figure 3(b) shows the rescaled maximum deflection $C^2 \delta_{\text{max}}$ as a function of inverse stiffness $1/\mathcal{E}$. The results collapse onto a straight line, consistent with the asymptotic prediction that $\delta_{\text{max}} \propto (\mathcal{E}C^2)^{-1}$, which follows from the balance between the hydrodynamic pressure load and the bending stiffness of the wall. The combination $\mathcal{E}C^2$ therefore acts as an effective stiffness-geometry parameter controlling deformation amplitude. A similar collapse is evident in Fig. 3(c), where the normalized flux deficit $(Q_{\text{rigid}} - Q)/Q_{\text{rigid}}$ is plotted against C^2/\mathcal{E} . Data across all curvatures merge onto a single curve, confirming that flow suppression depends primarily on this composite parameter (equivalently $(\mathcal{E}C^2)^{-1}$). The observed scaling remains valid within the lubrication approximation ($H_0/L \ll 1$) and under the thin-double-layer assumption ($\kappa H_0 \gg 1$) used in the theoretical formulation.

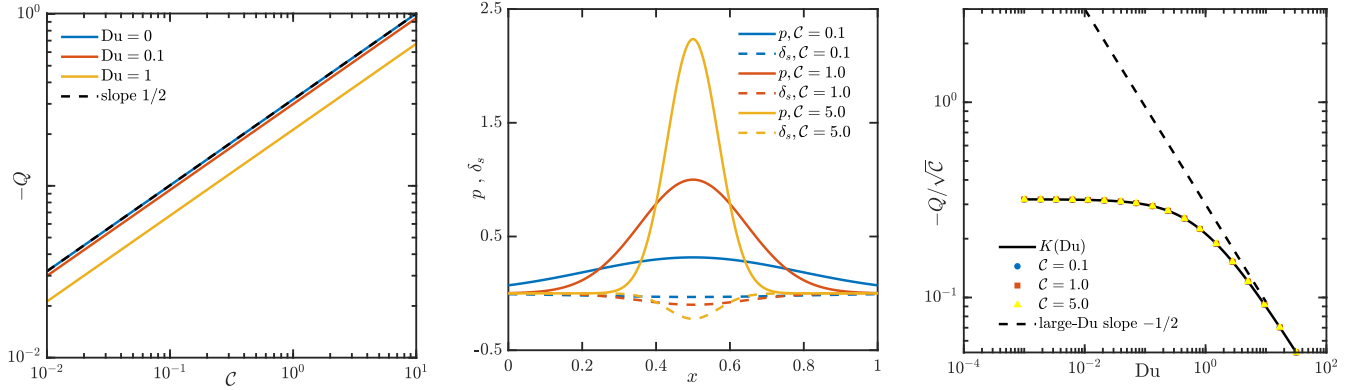


Figure 4: (a) Normalized flux ($-Q$) versus curvature (C) on loglog axes for several (Du), confirming the scaling ($Q \propto \sqrt{C}, K(Du)$) with slope (1/2). (b) Axial profiles of pressure $p(x)$ (solid) and wall deformation $\delta_s(x)$ (dashed) for $C = 0.15$, showing increasing localization near the throat and the onset of mild backflow at large (C). (c) Collapse of the normalized flux $-Q/\sqrt{C}$ onto the mobility function $K(Du)$; the dashed line indicates the asymptotic large- Du power-law scaling with exponent $-1/2$.

5.2 Effect of Geometric modulation

Curvature modifies electroosmotic transport through two concurrent mechanisms. Increasing C enhances the local electric field near the constriction due to geometric focusing, thereby amplifying electroosmotic slip. Simultaneously, the stronger curvature localizes the pressure and deformation fields, producing large gradients near the throat. The net flux thus results from the competition between enhanced electroosmotic driving and increased hydrodynamic resistance. Figure 4(a) depicts that the total flux follows the asymptotic scaling $Q \propto \sqrt{C} \mathcal{K}(Du)$, where $\mathcal{K}(Du)$ is a dimensionless function representing the influence of surface conduction. The loglog slope of 1/2 agrees with the analytical result derived from Eq. (25), confirming that throughput increases sublinearly with curvature. The physical origin of this dependence lies in the focusing of the electric field: as the constriction sharpens, the potential drop is distributed over a smaller region, increasing the local field intensity and hence the slip velocity. This geometric focusing effect compensates for, and at moderate curvatures exceeds, the rise in viscous resistance.

The axial profiles in Fig. 4(b) shows that with increasing C , pressure and deflection become increasingly localized near the throat. For highly compliant configurations, small adverse-pressure segments appear, indicating mild backflow zones associated with the elastic response. Figure 4(c) demonstrates that when Q/\sqrt{C} is plotted against the Dukhin number, data for different curvatures collapse onto a universal curve corresponding to $\mathcal{K}(Du)$. The asymptotic slope of $-1/2$ at large Du captures the suppression of electroosmotic transport due to dominant surface conduction, which effectively short-circuits the bulk current.

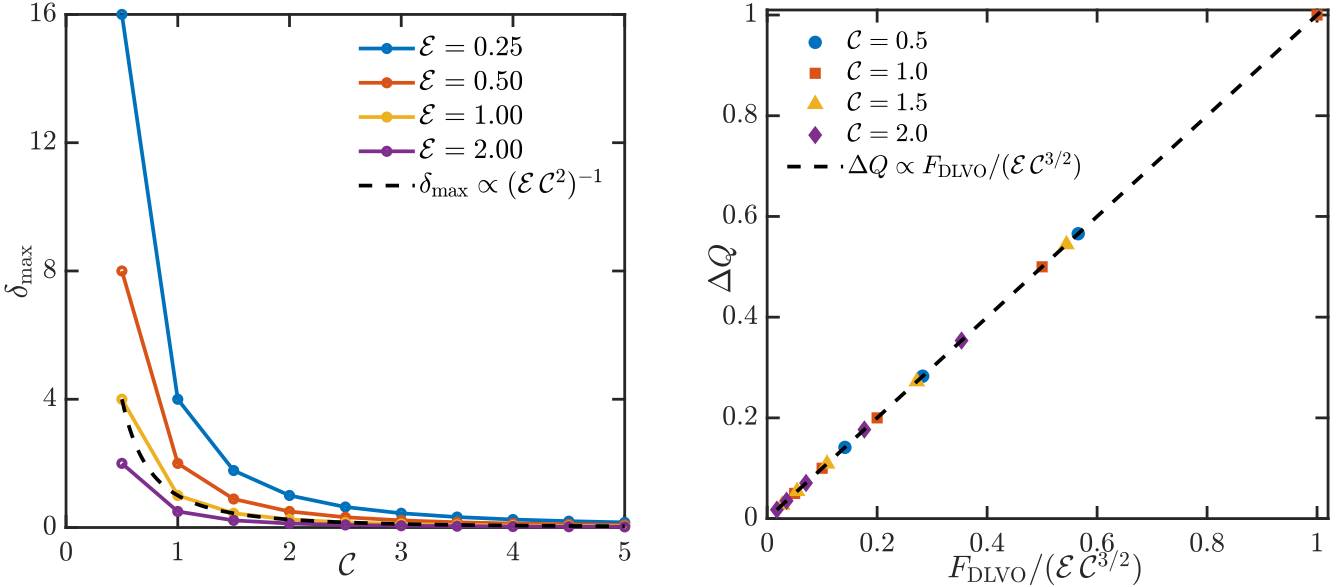


Figure 5: (a) Maximum deformation δ_{\max} as a function of curvature C for several wall stiffnesses \mathcal{E} . All curves exhibit the predicted C^{-2} decay, with a measured slope of -2.01 ± 0.05 . (b) Flux variation ΔQ plotted against the rescaled DLVO forcing $F_{\text{DLVO}}/(\mathcal{E} C^{3/2})$. The data collapse onto a single line with slope 1.00 ± 0.03 , confirming the asymptotic relation $\Delta Q \propto F_{\text{DLVO}}/(\mathcal{E} C^{3/2})$.

5.3 Narrow-gap scalings

In the narrow-gap regime, the balance between DLVO stresses and elastic resistance dominates the flow modulation. The asymptotic analysis in Sec. 3.4 predicts the scaling relations

$$\delta_{\max} \sim (\mathcal{E} C^2)^{-1}, \quad \Delta Q \sim \frac{F_{\text{DLVO}}}{\mathcal{E} C^{3/2}},$$

where F_{DLVO} denotes the characteristic DLVO forcing. Figure 5(a) shows that the numerically obtained deflections follow the power-law dependence $\delta_{\max} \sim C^{-2}$ with a fitted slope of -2.01 ± 0.05 and $R^2 > 0.99$. Figure 5(b) shows that the corresponding flux variation ΔQ scales linearly with $F_{\text{DLVO}}/(\mathcal{E} C^{3/2})$ with slope 1.00 ± 0.03 , in excellent agreement with the theoretical prediction.

These results demonstrate that the deformation amplitude is set by the elastic response to DLVO-induced normal stresses, while the reduction in throughput results from the coupling between the local narrowing of the gap and the global electrical resistance. Increasing either \mathcal{E} or C suppresses deformation by reducing wall compliance or amplifying the effective bending stiffness, respectively. Conversely, stronger electrostatic or van der Waals interactions increase F_{DLVO} and enhance the local deformation, but the exponential repulsion ultimately stabilizes the configuration against collapse. The difference in scaling exponents for δ_{\max} and ΔQ reflects that deformation is determined by local stress balance, whereas the flux change depends on global conductance modification.

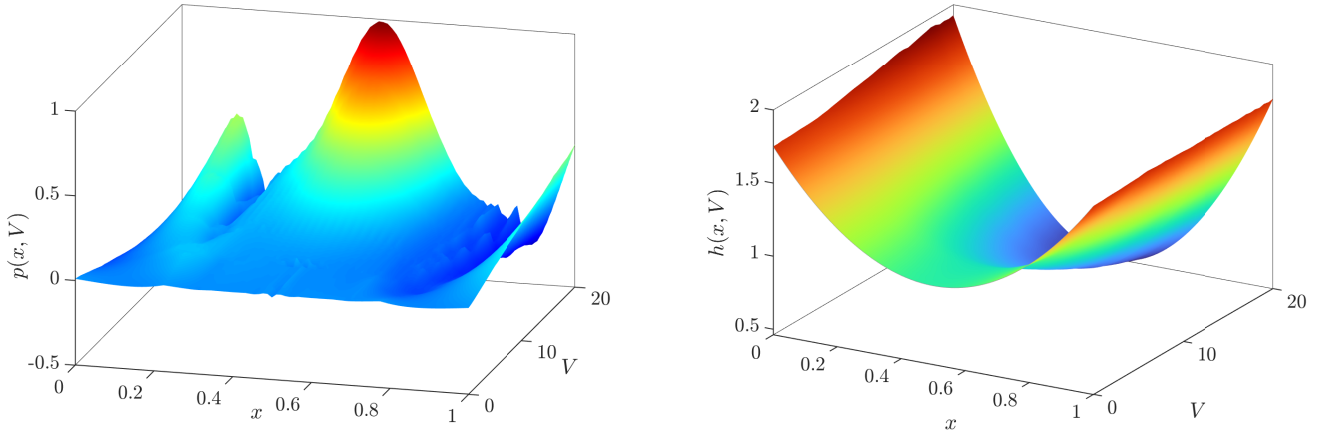


Figure 6: Voltage-induced pressure and deformation surfaces for a representative compliant channel. (a) Pressure surface $p(x, V)$ showing field focusing and pressure localization with increasing V . (b) Gap surface $h(x, V)$ exhibiting voltage-driven narrowing and high- V saturation due to DLVO repulsion. Together these surfaces highlight the coupled electrohydromechanical response: rising voltage amplifies electroosmotic forcing and pressure buildup, while elasticity and intermolecular repulsion bound the deformation.

5.4 Voltage-dependent deformation and pressure surfaces

The coupled electrohydromechanical response is presented in Figs. 6 and 7, which correspond to the pressure and deformation fields as functions of axial position and applied voltage. Figure 6(a) shows the variation of pressure $p(x, V)$, which intensifies and becomes increasingly localized near the throat as V increases. This localization of pressure has a large influence on the resulting electric-field focusing and the corresponding buildup of electroosmotic and Maxwell stresses. Figure 6(b) shows the associated gap surface $h(x, V)$. At low potentials ($V \lesssim 5$), the deformation varies almost linearly with V , indicating an elastically dominated response in which wall deflection scales directly with electroosmotic forcing. In this regime, the field remains approximately uniform and pressure gradients are weak. As V increases, nonlinear effects emerge: the accumulation of surface charge and the growth of Maxwell stresses lead to localized thinning near the midplane, marking the deformation-limited regime. In this regime, the elastic restoring stress increasingly counteracts the electrostatic load, producing pronounced curvature in $h(x, V)$. Beyond a threshold potential ($V \gtrsim 12$ –15), deformation saturates as DLVO repulsion dominates, establishing a repulsion-stabilized state.

Figure 7 captures these transitions on a single surface map. The steep gradients in $h(x, V)$ correspond to strong field focusing and rapid pressure buildup, while the flattened high-voltage region signifies self-limiting deformation controlled by the exponential repulsive term in the DLVO potential. This saturation indicates that even under large applied voltages, the compliant channel maintains a finite equilibrium gap determined by the balance between elastic bending energy and electrostatic repulsion.

Moreover, these results reveal a coherent picture of electroosmotic transport in compliant ge-

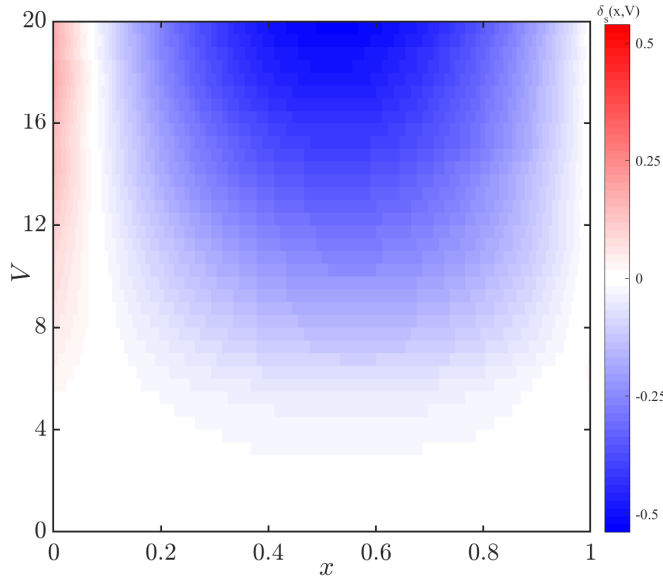


Figure 7: Voltage-induced deformation surface $h(x, V)$ in a compliant channel. The colormap shows the normalized gap variation $\delta(x, V)$. Low voltages produce small-amplitude, approximately linear deformation (orange), followed by a deformation-limited regime (white), and ultimately a DLVO-stabilized plateau at high voltages (blue). The surface curvature and slope highlight regions of electric-field focusing and pressure localization.

ometries. The overall behavior can be understood as a competition among three energy scales: the electroosmotic driving energy associated with the applied potential, the elastic strain energy of the deformable wall, and the intermolecular potential energy arising from DLVO interactions. At low forcing, the elastic energy dominates, leading to quasi-linear deformation. At intermediate voltages, the electroosmotic energy becomes comparable to the elastic energy, producing nonlinear confinement and pressure localization. At high voltages, the exponential DLVO repulsion overtakes both, resulting in saturation of deformation and stable operation. This self-limiting mechanism ensures that compliant electroosmotic channels do not collapse under strong fields, providing intrinsic robustness. The scaling relations derived here, particularly the dependence of deformation and flux on combined stiffness-curvature parameters such as $\mathcal{E}C^2$, furnish design rules for electroactive micro- and nanofluidic devices. By appropriately selecting wall stiffness, geometric curvature, and electrolyte composition, one can tailor the operating regime from linear stiff-wall response to voltage-tunable, repulsion-stabilized confinement and thereby enable controlled fluid regulation in soft electrokinetic systems.

6 Conclusions

We have developed and analyzed a nonlinear framework for electroosmotic lubrication in curved microchannels with a compliant wall, incorporating shortrange intermolecular interactions through an extended DLVO model. The formulation unifies electroosmotic slip, lubrication pressure, elastic

deformation, and molecular forces into a single description of confined electrokinetic transport.

Simulated results, supported by asymptotic analysis, outlay three qualitatively distinct regimes. In the stiff wall limit, wall deflection is negligible, and throughput responds linearly to the applied potential. At intermediate compliance, elastic narrowing throttles the channel, defining a deformation-limited regime where flow transport is constrained primarily by geometry. At very low stiffness, the DLVO repulsion provides intrinsic stabilization, capping deflection, and prevents collapse, even under the strong confinements. Across these regimes, the analysis identifies compact scaling relations in the strong constriction limit,

$$\delta_{\max} \sim \frac{F_{\text{DLVO}}}{\mathcal{E}\mathcal{C}^2}, \quad \Delta Q \sim \frac{F_{\text{DLVO}}}{\mathcal{E}\mathcal{C}^{3/2}}, \quad Q \sim -\sqrt{\mathcal{C}} \mathcal{K}(Du),$$

which were validated by numerical simulations. Physically, elasticity determines the amplitude of deformation, while curvature enhances throughput through voltage-driven field focusing while sharpening localization, and DLVO forces regulate confinement by balancing exponential repulsion and algebraic attraction. These mechanisms compress the complexity of the nonlinear coupled system into predictive design rules.

Furthermore, the results can also be used to predict the design of soft microfluidic and iontronic channels. By tuning wall compliance, constriction curvature, and electrolyte composition, one may deliberately shift operation between regimes to achieve targeted performance: stiff designs for linear response, compliant geometries for flow regulation, or soft channels stabilised by electrostatic repulsion. The corrected scaling relations provide simple yet quantitatively consistent design rules: stiffening or sharpening suppresses deflection, whereas stronger intermolecular forces amplify both deformation and flux suppression. More broadly, the identification of distinct stiff-wall, deformation-limited, and repulsion-limited regimes offers a unified framework for interpreting experimental observations in compliant electrokinetic systems.

Acknowledgments

S. Sahoo gratefully acknowledges the financial support received from the Ministry of Human Resource Development (MHRD), Government of India. A. K. Nayak thanks the NBHM, India, and the Science and Engineering Research Board (SERB), India (Grant No. CRG/2023/006863), for their support during the preparation of this manuscript.

Data Availability

The data that support the findings of this study are available within the article.

Author Notes

The authors declare that they have no competing interests.

Appendix

A.1 Matched asymptotics for electroosmotic slip in the thin-EDL limit

In this appendix, we briefly justify the HelmholtzSmoluchowski slip condition Eq. (2) using matched asymptotics in the thinEDL limit, following classical electrohydrodynamic theory [3, 4]. We consider steady, unidirectional EOF in a parallel-plate geometry, with a symmetric $z : z$ electrolyte, assuming constant viscosity μ , permittivity ε , and temperature T . The channel has half-height H_0 , and the wall at $y = 0$ carries potential ζ , while the bulk is electrically neutral. The nondimensional Debye length is $\delta = \lambda_D/H_0 \ll 1$, where $\lambda_D = \sqrt{\varepsilon k_B T / (2z^2 e^2 n_0)}$ is the physical Debye length and n_0 is the bulk ion concentration. We define the stretched inner coordinate $\eta = y/\delta$ to resolve the EDL.

Inner region (EDL layer, $y = O(\delta)$): The electrostatic potential $\phi(\eta)$ satisfies the PoissonBoltzmann equation:

$$\frac{d^2\phi}{d\eta^2} = \sinh \phi, \quad \phi(0) = \zeta^*, \quad \phi(\infty) = 0, \quad (\text{A.1})$$

where ϕ is scaled by the thermal voltage $k_B T/(ze)$ and $\zeta^* = ze\zeta/(k_B T)$. The fluid velocity $u(\eta)$ satisfies the Stokes equation with electrostatic forcing:

$$\frac{d^2u}{d\eta^2} = -E_x \frac{d\phi}{d\eta}, \quad (\text{A.2})$$

subject to no-slip at the wall $u(0) = 0$, and matching to the outer region as $\eta \rightarrow \infty$. Integrating Eq. (A.2) twice and applying boundary conditions gives:

$$u(\infty) = -E_x \int_0^\infty \phi(\eta) d\eta, \quad (\text{A.3})$$

which defines the electroosmotic slip velocity at the edge of the EDL.

Outer region (bulk, $y = O(1)$): The bulk is electroneutral, so $\nabla^2\phi = 0 \Rightarrow \phi \equiv 0$ at leading order. The velocity $u(y)$ satisfies $\mu d^2u/dy^2 = 0$, with the wall slip boundary condition

$$u|_{y=0} = u_{\text{slip}} = -E_x \int_0^\infty \phi(\eta) d\eta = -\frac{\varepsilon \zeta}{\mu} E_x, \quad (\text{A.4})$$

where the last identity holds under the DebyeHückel approximation or for weak potentials. This matched asymptotic analysis shows that, in the limit $\delta \rightarrow 0$, the inner problem collapses to a slip condition for the outer flow. The resulting HelmholtzSmoluchowski slip law is valid to leading order in δ , with corrections of $O(\delta)$ negligible for $\kappa^* = 1/\delta \gg 1$.

A.2 Derivation of the first-order flux correction (Eq. 22)

We start from the nondimensional flux law written with the augmented pressure P ,

$$Q = -\frac{h^3(x)}{12} \frac{dP}{dx} - \frac{\alpha h(x)}{h(x) + 2Du}, \quad P = P_0 + \varepsilon P_1, \quad h = h_0 - \varepsilon \delta_1, \quad \alpha = \alpha_0 + \varepsilon \alpha_1,$$

where

$$P_0 = p_0 + \mathcal{R}_e e^{-\kappa^* h_0} - \frac{\mathcal{R}_v}{h_0^3}, \quad P_1 = p_1 + \delta_1 K_{\text{DLVO}}, \quad K_{\text{DLVO}} = \kappa^* \mathcal{R}_e e^{-\kappa^* h_0} - \frac{3\mathcal{R}_v}{h_0^4}.$$

Poiseuille contribution. Using $(h_0 - \varepsilon \delta_1)^3 = h_0^3 - 3\varepsilon h_0^2 \delta_1 + O(\varepsilon^2)$ and $P' = P'_0 + \varepsilon P'_1$, we obtain

$$-\frac{h^3}{12} P' = -\frac{h_0^3}{12} P'_0 + \varepsilon \left[-\frac{h_0^3}{12} P'_1 + \frac{h_0^2 \delta_1}{4} P'_0 \right] + O(\varepsilon^2).$$

Electroosmotic contribution. Expand the EO term about h_0 and α_0 :

$$-\frac{\alpha h}{h + 2Du} = -\frac{\alpha_0 h_0}{h_0 + 2Du} + \varepsilon \left[\underbrace{\delta_1 \frac{2\alpha_0 Du}{(h_0 + 2Du)^2}}_{\text{local } h\text{-variation}} - \underbrace{\frac{h_0}{h_0 + 2Du} \alpha_1}_{\text{global } \alpha\text{-variation}} \right] + O(\varepsilon^2),$$

since $\frac{d}{dh} \left(-\alpha_0 \frac{h}{h+2Du} \right) \big|_{h_0} = -\alpha_0 \frac{2Du}{(h_0+2Du)^2}$ and $h = h_0 - \varepsilon \delta_1$.

Voltage constraint and α_1 . From

$$\alpha = \left(\int_0^1 \frac{dx}{h + 2Du} \right)^{-1}, \quad \frac{1}{h + 2Du} = \frac{1}{h_0 + 2Du} + \varepsilon \frac{\delta_1}{(h_0 + 2Du)^2} + O(\varepsilon^2),$$

we write $I = \int_0^1 (h + 2Du)^{-1} dx = I_0 + \varepsilon I_1 + \dots$ with

$$I_0 = \int_0^1 \frac{dx}{h_0 + 2Du}, \quad I_1 = \int_0^1 \frac{\delta_1(x)}{(h_0(x) + 2Du)^2} dx,$$

so that

$$\alpha = \frac{1}{I} = \alpha_0 + \varepsilon \alpha_1 + \dots, \quad \alpha_0 = \frac{1}{I_0}, \quad \alpha_1 = -\alpha_0^2 I_1 = -\alpha_0^2 \int_0^1 \frac{\delta_1(x)}{(h_0(x) + 2Du)^2} dx.$$

Collecting orders. Combining the Poiseuille and EO pieces gives

$$Q = Q_0 + \varepsilon q_1(x) + O(\varepsilon^2),$$

with

$$Q_0 = -\frac{h_0^3}{12} P'_0 - \frac{\alpha_0 h_0}{h_0 + 2Du},$$

and

$$q_1(x) = -\frac{h_0^3}{12} P'_1(x) + \frac{h_0^2 \delta_1}{4} P'_0(x) + \delta_1(x) \frac{2\alpha_0 Du}{(h_0 + 2Du)^2} - \frac{h_0}{h_0 + 2Du} \alpha_1,$$

which is Eq. (22). Since Q is spatially uniform, the constant Q_1 follows by enforcing compatibility (e.g. integrating q_1 over $x \in [0, 1]$); for equal end gaps the boundary terms from the P'_1 piece cancel, and in the Ohmic limit $Du \rightarrow 0$ the local EO correction vanishes, leaving only the global shift $-\alpha_1$.

A.3 Nomenclature

Dimensional symbols

Symbol	Description	Units
x	Axial coordinate	m
L	Channel length	m
X_c	Location of constriction apex	m
$h(x)$	Local gap height	m
H_0	Minimum undeformed gap	m
R	Radius of curvature of upper wall	m
$\delta_s(x)$	Downward wall deflection	m
$p(x)$	Hydrodynamic pressure	Pa
$P(x)$	Augmented pressure $p + p_{\text{DLVO}}$	Pa
$p_{\text{DLVO}}(h)$	DLVO disjoining pressure	Pa
$q(x)$	Volumetric flux per unit width	m^2/s
Q	Constant (conserved) flux	m^2/s
u_{eo}	Electroosmotic slip velocity	m/s
U_{eo}	EO velocity scale, $\varepsilon\zeta\Delta\phi/(\mu L)$	m/s
E_x	Axial electric field	V/m
$\Delta\phi$	Applied potential drop	V
ζ	Zeta potential	V
ε	Permittivity	F/m
μ	Dynamic viscosity	Pas
σ_b	Bulk conductivity	S/m
K_s	Surface conductance (per wall)	S
z	Ion valence	
n_0	Bulk ion concentration	m^{-3}
k_B	Boltzmann constant	J/K
T	Temperature	K
e	Elementary charge	C
ψ_0	Surface potential	V
κ	Inverse Debye length	m^{-1}
λ_D	Debye length	m
A_H	Hamaker constant	J
h_s	Thickness of compliant wall	m
E_Y	Youngs modulus	Pa
ν	Poissons ratio	
D	Flexural rigidity	Nm

Dimensionless variables and parameters

Symbol	Description	Definition
x	Axial coordinate	x/L
x_c	Constriction location	X_c/L
h	Gap	h/H_0
δ_s	Wall deflection	δ_s/H_0
p	Pressure	$p/(\mu U_{eo} L/H_0^2)$
q	Flux	$q/(U_{eo} H_0)$
Q	Conserved flux	
\mathcal{C}	Curvature parameter	$L^2/(2RH_0)$
κ^*	Scaled inverse Debye length	κH_0
Du	Dukhin number	$K_s/(\sigma_b H_0)$
\mathcal{R}_e	Electrostatic repulsion strength	see text
\mathcal{R}_v	van der Waals attraction strength	see text
\mathcal{E}	Compliance parameter	$DH_0^3/(\mu U_{eo} L^5)$
$P(x)$	Augmented pressure (dimensionless)	$p + \mathcal{R}_e e^{-\kappa^* h} - \mathcal{R}_v/h^3$

Auxiliary / asymptotic notation

Symbol	Meaning / Notes
Q law	$Q = -\frac{h^3}{12} dP/dx - \frac{\alpha h}{h+2Du}$
α	Global EO factor $(\int_0^1 (h+2Du)^{-1} dx)^{-1}$
α_0, α_1	Leading and $O(\varepsilon)$ terms in α expansion
Beam balance	$P(x) = \mathcal{E} d^4 \delta_s / dx^4$
ε	Small parameter $1/\mathcal{E}$ (distinct from permittivity)
$h_0(x)$	Base gap $1 + \mathcal{C}(x - x_c)^2$
p_0, p_1	Asymptotic pressures
δ_1	First-order wall deflection
K_{DLVO}	Incremental stiffness $\kappa^* \mathcal{R}_e e^{-\kappa^* h_0} - 3\mathcal{R}_v/h_0^4$
ξ	Stretched coordinate $\sqrt{\mathcal{C}}(x - x_c)$
δ_{\max}	Maximum deflection scaling $\propto (\mathcal{E} \mathcal{C}^2)^{-1}$
h_c	Critical gap from $\mathcal{R}_e e^{-\kappa^* h_c} = \mathcal{R}_v/h_c^3$

References

- [1] Saville, D. A. (1977). Electrokinetic effects with small particles. *Annual Review of Fluid Mechanics*, 9(1), 321-337.
- [2] Ren, L., Qu, W., & Li, D. (2001). Interfacial electrokinetic effects on liquid flow in microchannels. *International journal of heat and mass transfer*, 44(16), 3125-3134.
- [3] Probstein, R. F. (2005). *Physicochemical hydrodynamics: an introduction*. John Wiley & Sons.

- [4] Hunter, R. J. (2013). *Zeta potential in colloid science: principles and applications* (Vol. 2). Academic press.
- [5] Schnitzer, O., & Yariv, E. (2012). Induced-charge electro-osmosis beyond weak fields. *Physical Review E Statistical, Nonlinear, and Soft Matter Physics*, 86(6), 061506.
- [6] Wong, P. K., Wang, T. H., Deval, J. H., & Ho, C. M. (2004). Electrokinetics in micro devices for biotechnology applications. *IEEE/ASME transactions on mechatronics*, 9(2), 366-376.
- [7] Fiechtner, G. J., & Cummings, E. B. (2003). Faceted design of channels for low-dispersion electrokinetic flows in microfluidic systems. *Analytical Chemistry*, 75(18), 4747-4755.
- [8] Fernández-Mateo, R., Calero, V., Morgan, H., Ramos, A., & García-Sánchez, P. (2021). Concentrationpolarization electroosmosis near insulating constrictions within microfluidic channels. *Analytical Chemistry*, 93(44), 14667-14674.
- [9] Koyama, S., Inoue, D., Okada, A., & Yoshida, H. (2021). Electro-osmotic diode based on colloidal nano-valves between double membranes. *Physical Review Research*, 3(3), 033289.
- [10] Gu, Z., Huo, P., Xu, B., Su, M., Bazant, M. Z., & Deng, D. (2022). Electrokinetics in two-dimensional complicated geometries: Conformal mapping and experimental comparison. *Physical Review Fluids*, 7(3), 033701.
- [11] Chakraborty, D., Prakash, J. R., Friend, J., & Yeo, L. (2012). Fluid-structure interaction in deformable microchannels. *Physics of Fluids*, 24(10).
- [12] Yu, H., & Zhou, G. (2013). Deformable mold based on-demand microchannel fabrication technology. *Sensors and Actuators B: Chemical*, 183, 40-45.
- [13] Ozsun, O., Yakhot, V., & Ekinci, K. L. (2013). Non-invasive measurement of the pressure distribution in a deformable micro-channel. *Journal of Fluid Mechanics*, 734, R1.
- [14] Mehboudi, A., & Yeom, J. (2018). A one-dimensional model for compressible fluid flows through deformable microchannels. *Physics of Fluids*, 30(9).
- [15] Wang, X., & Christov, I. C. (2019). Theory of the flow-induced deformation of shallow compliant microchannels with thick walls. *Proceedings of the Royal Society A*, 475(2231), 20190513.
- [16] Guyard, G., Restagno, F., & McGraw, J. D. (2022). Elastohydrodynamic relaxation of soft and deformable microchannels. *Physical review letters*, 129(20), 204501.
- [17] Greidanus, A. J., Delfos, R., Picken, S. J., & Westerweel, J. (2022). Response regimes in the fluidstructure interaction of wall turbulence over a compliant coating. *Journal of Fluid Mechanics*, 952, A1.
- [18] Roy, A., & Dhar, P. (2024). Fluidstructure-interactive elasto-and thermo-hydrodynamics of electrokinetic binary fluid flows in compliant micro-confinements. *Physics of Fluids*, 36(3).

[19] Essink, M. H., Pandey, A., Karpitschka, S., Venner, C. H., & Snoeijer, J. H. (2021). Regimes of soft lubrication. *Journal of fluid mechanics*, 915, A49.

[20] Karan, P., Chakraborty, J., & Chakraborty, S. (2021). Generalization of elastohydrodynamic interactions between a rigid sphere and a nearby soft wall. *Journal of Fluid Mechanics*, 923, A32.

[21] Ghosal, S. (2002). Lubrication theory for electro-osmotic flow in a microfluidic channel of slowly varying cross-section and wall charge. *Journal of Fluid Mechanics*, 459, 103-128.

[22] Shit, G. C., Sengupta, A., & Mondal, P. K. (2024). Stability analysis of electro-osmotic flow in a rotating microchannel. *Journal of Fluid Mechanics*, 983, A13.

[23] Goyal, V., Datta, S., & Chakraborty, S. (2024). Generalizing electroosmotic-flow predictions over charge-modulated periodic topographies: tuneable far-field effects. *Journal of Fluid Mechanics*, 990, A1.

[24] Skotheim, J. M., & Mahadevan, L. (2005). Soft lubrication: The elastohydrodynamics of nonconforming and conforming contacts. *Physics of Fluids*, 17(9).

[25] Skotheim, J. M., & Mahadevan, L. (2004). Dynamics of poroelastic filaments. *Proceedings of the Royal Society A*, 460(2047), 1995-2020.

[26] Skotheim, J. M., & Mahadevan, L. (2004). Soft lubrication. *Physical review letters*, 92(24), 245509.

[27] Salez, T., & Mahadevan, L. (2015). Elastohydrodynamics of a sliding, spinning and sedimenting cylinder near a soft wall. *Journal of Fluid Mechanics*, 779, 181-196.

[28] Bertin, V., Amarouchene, Y., Raphaël, E., & Salez, T. (2022). Soft-lubrication interactions between a rigid sphere and an elastic wall. *Journal of Fluid Mechanics*, 933, A23.

[29] Rallabandi, B. (2024). Fluid-elastic interactions near contact at low Reynolds number. *Annual Review of Fluid Mechanics*, 56(1), 491-519.

[30] Bharti, Ferreira, Q., Jha, A., Carlson, A., Dean, D. S., Amarouchene, Y., Chan, T. S., & Salez, T. (2024). Singular viscoelastic perturbation to soft lubrication. *Physical Review Research*, 6(4), 043060.

[31] Paludan, M. V., Dollet, B., Marmottant, P., & Jensen, K. H. (2024). Elastohydrodynamic interactions in soft hydraulic knots. *Journal of Fluid Mechanics*, 984, A55.

[32] Fares, N., Lavaud, M., Zhang, Z., Jha, A., Amarouchene, Y., & Salez, T. (2024). Observation of Brownian elastohydrodynamic forces acting on confined soft colloids. *Proceedings of the National Academy of Sciences*, 121(42), e2411956121.

[33] Wang, Y., Dhong, C., & Frechette, J. (2015). Out-of-contact elastohydrodynamic deformation due to lubrication forces. *Physical Review Letters*, 115(24), 248302.

- [34] Davies-Strickleton, H., Débarre, D., El Amri, N., Verdier, C., Richter, R. P., & Bureau, L. (2018). Elastohydrodynamic lift at a soft wall. *Physical Review Letters*, 120(19), 198001.
- [35] Ding, L. (2025). Long-time asymptotics of passive scalar transport in periodically modulated channels. *Journal of Fluid Mechanics*, 1023, A19. doi:10.1017/jfm.2025.10814.
- [36] Ding, L. (2023). Shear dispersion of multispecies electrolyte solutions in the channel domain. *Journal of Fluid Mechanics*, 970, A27
- [37] Wang, X., & Christov, I. C. (2022). Reduced modelling and global instability of finite-Reynolds-number flow in compliant rectangular channels. *Journal of Fluid Mechanics*, 950, A26.
- [38] Martínez-Calvo, A., Sevilla, A., Peng, G. G., & Stone, H. A. (2020). Start-up flow in shallow deformable microchannels. *Journal of Fluid Mechanics*, 885, A25.
- [39] Inamdar, T. C., Wang, X., & Christov, I. C. (2020). Unsteady fluid-structure interactions in a soft-walled microchannel: A one-dimensional lubrication model for finite Reynolds number. *Physical Review Fluids*, 5(6), 064101.
- [40] Ramos-Arzola, L., & Bautista, O. (2021). Fluid structure-interaction in a deformable microchannel conveying a viscoelastic fluid. *Journal of Non-Newtonian Fluid Mechanics*, 296, 104634.
- [41] Boyko, E., Stone, H. A., & Christov, I. C. (2022). Flow ratepressure drop relation for deformable channels via fluidic and elastic reciprocal theorems. *Physical Review Fluids*, 7(9), L092201.
- [42] Gervais, T., El-Ali, J., Günther, A., & Jensen, K. F. (2006). Flow-induced deformation of shallow microfluidic channels. *Lab on a Chip*, 6(4), 500-507.
- [43] Chun, S., Christov, I. C., & Feng, J. (2025). Experimental investigation of the flow ratepressure drop relation of a viscoelastic Boger fluid in a deformable channel. *Physical Review Applied*, 24(3), 034001.
- [44] Keiser, L., Marmottant, P., & Dollet, B. (2022). Intermittent air invasion in pervaporating compliant microchannels. *Journal of Fluid Mechanics*, 948, A52.
- [45] Boyko, E., & Christov, I. C. (2023). Non-Newtonian fluidstructure interaction: Flow of a viscoelastic Oldroyd-B fluid in a deformable channel. *Journal of Non-Newtonian Fluid Mechanics*, 313, 104990.
- [46] Chun, S., Boyko, E., Christov, I. C., & Feng, J. (2024). Flow ratepressure drop relations for shear-thinning fluids in deformable configurations: Theory and experiments. *Physical Review Fluids*, 9(4), 043302.
- [47] Boyko, E. (2025). Interplay between complex fluid rheology and wall compliance in the flow resistance of deformable axisymmetric configurations. *Journal of Non-Newtonian Fluid Mechanics*, 336, 105380.

[48] Green, Y. (2022). Effects of surface-charge regulation, convection, and slip lengths on the electrical conductance of charged nanopores. *Physical Review Fluids*, 7(1), 013702.

[49] Chakraborty, J., & Chakraborty, S. (2010). Influence of streaming potential on the elastic response of a compliant microfluidic substrate subjected to dynamic loading. *Physics of Fluids*, 22(12).

[50] Matse, M., Berg, P., & Eikerling, M. (2018). Counterion flow through a deformable and charged nanochannel. *Physical Review E*, 98(5), 053101.

[51] Mandal, S., Ghosh, U., Bandopadhyay, A., & Chakraborty, S. (2015). Electro-osmosis of superimposed fluids in the presence of modulated charged surfaces in narrow confinements. *Journal of Fluid Mechanics*, 776, 390-429.

[52] Pal, S. K., Mahapatra, P., Ohshima, H., & Gopmandal, P. P. (2024). Electroosmotic flow modulation and enhanced mixing through a soft nanochannel with patterned wall charge and hydrodynamic slippage. *Industrial & Engineering Chemistry Research*, 63(29), 12977-12998.

[53] Mukherjee, S., Dhar, J., DasGupta, S., & Chakraborty, S. (2022). Electrokinetically augmented load bearing capacity of a deformable microfluidic channel. *Physics of Fluids*, 34(8).

[54] Boyko, E., Ilssar, D., Bercovici, M., & Gat, A. D. (2020). Interfacial instability of thin films in soft microfluidic configurations actuated by electro-osmotic flow. *Physical Review Fluids*, 5(10), 104201.

[55] Bhaskaran, A. M., Agrawal, S., Sarkar, K., & Dhar, P. (2024). Elasto-compliance of harmonically stimulated soft micro-gaps during electro-magneto-kinetic flows. *Soft Matter*, 20(30), 5969-5982.

[56] Maroundik, N., Ilssar, D., & Boyko, E. (2025). Diffusioosmotic flow in a soft microfluidic configuration induces fluid-structure instability. *Physical Review Fluids*, 10(10), 104203.

[57] McNamee, C. E. (2019). Effect of a liquid flow on the forces between charged solid surfaces and the non-equilibrium electric double layer. *Advances in Colloid and Interface Science*, 266, 21-33.

[58] Norouzisadeh, M., Leroy, P., & Soulaine, C. (2024). A lubrication model with slope-dependent disjoining pressure for modeling wettability alteration. *Computer Physics Communications*, 298, 109114.

[59] Yaros, H. D., Newman, J., & Radke, C. J. (2003). Evaluation of DLVO theory with disjoining-pressure and film-conductance measurements of common-black films stabilized with sodium dodecyl sulfate. *Journal of colloid and interface science*, 262(2), 442-455.

[60] Rodríguez, A., Arcos, J., Méndez, F., & Bautista, O. (2025). Gaseous slip flow through a shallow deformable microchannel. *Physics of Fluids*, 37(6).